Acta Pharmacologica Sinica

www.nature.com/aps

ARTICLE

Ras inhibitor farnesylthiosalicylic acid conjugated with IR783 dye exhibits improved tumor-targeting and altered anti-breast cancer mechanisms in mice

Qiu-ju Huang[1,2], Guo-chao Liao[1], Xue-rong Zhuang[1], Meng-lan Yang[1], Jing-jing Yao[1], Jian-hua Deng[1], Yan-min Zhang[1], Ying Wang[1], Xiao-xiao Qi[1], Dong-feng Pan[3], Yang Guan[1], Zhi-ying Huang[1], Feng-xue Zhang[2], Zhong-qiu Liu[1,4] and Lin-lin Lu[1,4]

Ras has long been viewed as a promising target for cancer therapy. Farnesylthiosalicylic acid (FTS), as the only Ras inhibitor has ever entered phase II clinical trials, has yielded disappointing results due to its strong hydrophobicity, poor tumor-targeting capacity, and low therapeutic efficiency. Thus, enhancing hydrophilicity and tumor-targeting capacity of FTS for improving its therapeutic efficacy is of great significance. In this study we conjugated FTS with a cancer-targeting small molecule dye IR783 and characterized the anticancer properties of the conjugate FTS-IR783. We showed that IR783 conjugation greatly improved the hydrophilicity, tumor-targeting and therapeutic potential of FTS. After a single oral administration in Balb/c mice, the relative bioavailability of FTS-IR783 was increased by 90.7% compared with FTS. We demonstrated that organic anion transporting polypeptide (OATP) and endocytosis synergistically drove the uptake of the FTS-IR783 conjugate in breast cancer MDA-MB-231 cells, resulting in superior tumor-targeting ability of the conjugate both in vitro and in vivo. We further revealed that FTS-IR783 conjugate could bind with and directly activate AMPK rather than affecting Ras, and subsequently regulate the TSC2/mTOR signaling pathway, thus achieving 2–10-fold increased anti-cancer therapeutic efficacy against 6 human breast cancer cell lines compared to FTS both in vivo and in vitro. Overall, our data highlights a promising approach for the modification of the anti-tumor drug FTS using IR783 and makes it possible to return FTS back to the clinic with a better efficacy.

Keywords: Ras inhibitor; Farnesylthiosalicylic acid; IR783; tumor-targeting; breast neoplasm; AMPK; mTOR

Acta Pharmacologica Sinica (2022) 43:1843–1856; https://doi.org/10.1038/s41401-021-00775-5

INTRODUCTION

Farnesylthiosalicylic acid (FTS), which is the only Ras inhibitor that has ever entered phase II clinical trials, has been considered the most promising Ras inhibitor for cancer therapy [1]. Up to ~30% of human tumors have been found to carry oncogenic RAS mutations, and Ras has long been viewed as a promising target for cancer therapy [2, 3]. Unfortunately, decades of research have yet to yield a Ras inhibitor that can successfully be used in clinical cancer therapy [4]. As a well-characterized small-molecule Ras inhibitor, FTS exhibited desirable killing effects on hematologic malignancies and solid tumors [5–7] by inhibiting the anchoring of Ras in the cellular membrane, subsequently suppressing the Ras downstream signaling pathways Raf/MEK/ERK and PI3K/Akt/mTOR [8, 9]. However, the results of clinical trials were disappointing for two main reasons: (i) the strong hydrophobicity of FTS limits the absorption of the drug, leading to low bioavailability even with high-dose oral treatment [10, 11] in patients who received up to 2000 mg of FTS per day (1000 mg twice daily); (ii) the poor tumor-targeting capacity caused poor therapeutic efficiency and widespread adverse reactions, especially for solid tumors, prohibiting the clinical application of FTS. In clinical trials, only 17%–33% of patients with solid tumors showed evidence of disease stabilization on FTS [5, 12]. Approximately 60%–85%, 68.4%, and 20%–40% of patients suffered from drug-related diarrhea, anemia, and abdominal pain, respectively [5, 11, 13]. Thus, the enhancement of the solubility and tumor-targeting capacity of FTS is a key issue for its continued application in clinical practice.

Near-infrared fluorescent (NIRF) haematocyanin dyes, including IR-780, IR783, IR-808, and MHI-148, have been recognized as ideal carriers for tumor imaging and targeted therapy [14, 15] because they have the following advantages. (i) They show good hydrophilicity and biocompatibility, which makes them good candidates for application in vivo. No systemic toxicity response was observed in C57BL/6 mice after injection of 37.5 $mg \cdot kg^{-1}$ IR783 (100 times the routine imaging dose) daily for 1 month [16]. (ii) Their strong signal strength and resistance to photobleaching allow their fluorescence to be readily detected in deep tissues.

[1]Joint Laboratory for Translational Cancer Research of Chinese Medicine of the Ministry of Education of the People's Republic of China, International Institute for Translational Chinese Medicine, Guangzhou University of Chinese Medicine, Guangzhou 510006, China; [2]School of Basic Medical Sciences, Guangzhou University of Chinese Medicine, Guangzhou 510006, China; [3]Department of Radiology and Medical Imaging, University of Virginia, Charlottesville, VA 22903, USA and [4]State Key Laboratory of Quality Research in Chinese Medicine/ Macau Institute for Applied Research in Medicine and Health, Macau University of Science and Technology, Macao, SAR, China
Correspondence: Zhong-qiu Liu (liuzq@gzucm.edu.cn) or Lin-lin Lu (lllu@gzucm.edu.cn)
These authors contributed equally: Qiu-ju Huang, Guo-chao Liao

Received: 6 April 2021 Accepted: 5 September 2021
Published online: 29 November 2021

Because it has the highest absorptivity ($\varepsilon = 261{,}000\ M^{-1} \cdot cm^{-1}$) and fluorescence efficiency ($\Phi Fl = 0.084$), IR783 was found to be the best candidate for NIRF tumor imaging among a series of NIRFs, cypate, ICG, and IR820 in a test of their absorbance/fluorescence properties [17]. (iii) Their high affinity towards tumors confers them with active tumor-targeting capacity. IR783 was found to accumulate in tumor tissues at 24 h and was retained even at 4 days without any accumulation in other vital organs of mice [16]. It has been reported that IR783 uptake could be mediated by transmembrane proteins of the organic anion transporting polypeptide family, such as OATP1 and OATP1B3 [18]. Thus, the NIRF dye IR783 is an ideal choice for the modification of cancer therapeutic drugs or candidates to improve their hydrophilicity and tumor-targeting ability.

Several successful studies have recently demonstrated that the NIRF dye IR783 could markedly improve cancer cell-targeted delivery and anticancer therapy using anticancer agents, including genistein and nanomedicines [19, 20]. Herein, the NIRF dye IR783 was used as a tumor-targeting delivery carrier after conjugation with FTS to overcome the problems faced when using FTS alone. However, the following questions with the use of FTS after conjugation with IR783 require answers: (i) Can the hydrophilicity and tumor-targeting ability of the conjugate be improved? (ii) Is the therapeutic efficacy of the conjugate enhanced? (iii) What are the tumor-targeting mechanism and intracellular distribution of the conjugates? (iv) Does the addition of IR783 change the target of FTS?

MATERIALS AND METHODS

Reagents, cell lines, and animals

FTS was purchased from Topscience (Shanghai, China). IR783, Sucrose, Chlorpromazine, Amiloride, Methyl-β-cyclodextrin, Dimethyl sulfoxide (DMSO), 3-[4, 5-dimethylthiazol-2-yl]-2, 5-diphenyltetrazolium bromide (MTT) and 1-octanol (the ACS reagent of ≥99% purity) were obtained from Sigma-Aldrich (Milwaukee, WI). Bromosulphophthalein (BSP) was purchased from Waterstone Technology (Carmel, IN, USA). Sincalide (cholecystokinin-8, CCK8), Hoechst 33342, KU-0063794 and MHY1485 were obtained from Med Chem Express (Monmouth Junction, NJ, USA). Estradiol-17β-glucuronide (E2G) was obtained from LGM Pharma (Nashville, TN, USA). Dorsomorphin was purchased from Aladdin Technologies Inc. (Shanghai, China). 4′,6-diamidino-2-phenylindole (DAPI) was purchased from GBCBIO Technologies Inc. (Guangzhou, China). Luciferin, Cell Light™ Golgi-GFP dye and ER-Tracker™ Green dye were obtained from Thermo Fisher (Waltham, MA, USA). Mito Tracker® Green FM, Lyso Tracker®Green DND-26, and primary antibodies Ras (1:1000, 3965S), E-cadherin (1:1000, 3195P), N-cadherin (1:1000, 13116T), Vimentin (1:1000, 5741T), Akt1 (1:1000, 75692S), p-Akt (S473) (1:1000, 4060T), mTOR (1:1000, 2983S), p-mTOR(2448) (1:1000, 5536T), p-mTOR(2481) (1:1000, 2974T), p70S6K (1:1000, 2708S), p-p70S6K (1:1000, 9234S), AMPKα (1:1000, 5832S), p-AMPKα (1:1000, 2535S), AMPKβ (1:1000, 4150T) and p-AMPKβ (1:1000, 4186T) were purchased from Cell Signaling Technology Inc. (Beverly, MA, USA). Primary antibody PCNA (1:1000, MAB424) was purchased from Merck Millipore (Darmstadt, Germany). Primary antibody Ki67 (Alexa Flour 488) (1:50, ab206633) was purchased from Abcam (Cambridge, UK). Primary antibodies β-actin (1:500, sc-81178), ERK1/2 (1:500, sc-292838), p-ERK1/2 (1:500, sc-7383), TSC2 (1:500, sc-271314), p-TSC2 (1:500, sc-293149) and secondly antibodies were purchased from Santa Cruz Biotechnology (Santa Cruz, CA, USA). Water was Millipore water of resistivity 18.2 MΩ · cm. Other solvents were of analytical grade and used as received.

The human breast cancer cell lines MDA-MB-231, BT-549, SK-BR-3, BT-474, and MCF-7, and the human mammary epithelial cell line MCF10A were purchased from the ATCC (Manassas, VA, USA). The mouse breast cancer fluorescent cell line 4T1-luc2 was purchased from Perkin Elmer (Waltham, MA, USA). MDA-MB-231 and MCF-7 cells were cultured in MEM supplemented with 10% FBS. BT-549, BT-474, and 4T1-luc2 cells were cultured in RPMI-1640 supplemented with 10% FBS. SK-BR-3 cells were cultured in DMEM supplemented with 10% FBS. MCF10A cells were cultured in GMEM complete medium supplemented with 100 ng mL^{-1} cholera toxin (Calbiochem, San Diego, CA). All cells were maintained in a humidified atmosphere with 5% CO_2 at 37 °C.

Female Balb/c mice (4–6 weeks, 18–22 g) and female Balb/c-nude mice (4–6 weeks, 16–20 g) were purchased from Laboratory Animal Center of Southern Medical University [License number: SCXK (Guangdong) 2016-0041; Guangzhou, China], and kept in the animal facility in the SPF animal laboratory [License number: SYXK (GZ) 2019-0144] at International Institute for Translational Chinese Medicine, Guangzhou University of Chinese Medicine (Guangzhou, China). All the animal experiments were approved by International Institute for Translational Chinese Medicine Animal Care and Use Committee, Guangzhou University of Chinese Medicine.

Synthesis and characterization of FTS-IR783 conjugate

Synthesis scheme of FTS-IR783 was shown in Fig. 1a. FTS (compound 1, 20.00 mg, 0.0558 mmol) was mixed with N-hydroxysuccinamide (7.70 mg, 0.0669 mmol) and dicyclohexylcarbodiimide (DCC, 13.82 mg, 0.0669 mmol) in methylene chloride, then dimethylaminopyridine was added (DMAP, 0.68 mg, 0.0056 mmol) and the mixture was stirred at room temperature for 2 h. Next, compound 2 (25.28 mg, 0.05578 mmol) was mixed with 2-aminoethanol (19.36 mg, 25.09 mmol) and *N*, *N*-diisopropylamine (DIEA, 0.05 mL, 0.30 mmol) in methylene chloride and stirred at room temperature for 2 h. Finally, compound 3 (22.00 mg, 0.055 mmol) was mixed with IR783 dye (41.20 mg, 0.055 mmol) and DIEA (0.02 mL, 0.12 mmol) in 4 mL methanol.

Characterizations of FTS-IR783 conjugate. (i) For NMR spectra: ^{13}C-NMR, ^{1}H-NMR, ^{13}C-^{1}H COSY and ^{1}H-^{1}H COSY spectra of compound 4 were obtained using AVANCE III HD 400 MHz Digital NMR Spectrometer (Bruker, Switzerland). ^{13}C-NMR (101 MHz, Chloroform-d), δ 171.86, 168.95, 142.21, 145.36, 141.98, 140.86, 135.50, 131.34, 124.94, 124.29, 123.74, 122.26, 118.33, 101.78, 110.56, 54.09, 49.13, 42.51, 39.69, 39.59, 32.37, 28.11, 26.72, 26.41, 26.08, 25.73, 22.78, 18.72, 17.72, 17.43, 16.03, 12.35. ^{1}H-NMR (400 MHz, Chloroform-d), δ 8.78 (d, J = 13.8 Hz, 1H, ArH), 7.63 (d, J = 7.7 Hz, 1H, NH), 7.53 (d, J = 10.2 Hz, 1H, ArH), 7.36 (t, J = 7.7 Hz, 2H, ArH), 7.31 (d, J = 8.0 Hz, 4H, ArH,), 7.20 (t, J = 7.2 Hz, 3H, ArH), 7.10 (d, J = 8.0 Hz, 2H, =CH), 6.28 (d, J = 14.0 Hz,1H, ArH) 5.21 (t, J = 7.7 Hz, 1H, =CH), 5.04 (dd, J = 12.7, 6.9 Hz, 2H, =CH), 4.09 (s, 2H, =CH2), 3.66 (pd, J = 6.6, 4.0 Hz, 6H, N-CH2), 3.47 (d, J = 7.7 Hz, 2H, =CH2), 3.10 (qd, J = 7.4, 4.0 Hz, 8H, S-CH2), 2.96 (s, 2H, -CH2), 2.67 (s, 2H, -CH2), 2.06 (s, 14H), 1.95–1.93 (m, 2H), 1.58 (s, 2H), 1.55 (s, 3H), 1.54 (s, 3H), 1.53 (s, 8H), 1.51 (s, 9H). (ii) For FT-IR spectra: the FT-IR spectra of compound 4 were recorded using a Thermo Scientific™ Nicolet™ iS50 FTIR Spectrometer (Thermo, USA) equipped with a KBr beamsplitter. The wave number range was 400–4000 cm^{-1}. The spectral resolution was 0.1 cm^{-1}. Background scans were acquired before sample analysis. (iii) For LC/MS/MS analysis: compound 4 (10 μM) was injected into a UPLC-DAD-QTOF with 6540 accurate-mass Q-TOF MS system (Agilent Technologies, Inc., CA, USA) for analysis. The chromatograph conditions were as follows: column, Agilent ZORBAX RRHD SB-C18 (3 × 100 mm, 1.8 μm); mobile phase A (0% ddH_2O, pH 2.5), mobile phase B, (100% acetonitrile); isocratic elution, 8 min; flow rate, 0.3 mL · min^{-1} and injection volume, 10 μL. The mass conditions were as follows: capillary voltage 3.5 kV, nozzle voltage 1.5 kV, sheath gas temperature 320 °C and desolvation temperature 350 °C with sheath gas flow of 8 L · min^{-1} and desolvation flow of 11 L · min^{-1}. DAD (diode array detector) scan range 190–400 nm, 50–1600 *m/z*. Electrospray ionization was performed in positive mode. Data were recorded and the system was controlled using the MassHunter software (version B.06.00, Agilent Technologies).

Partition coefficient and water solubility

FTS powder (0.36 mg) was dissolved in 0.50 mL 1-octanol with ultrasonic for 5 min, and then 0.50 mL water was added followed by vigorous mixing; FTS-IR783 powder (1.11 mg) was dissolved in 0.50 mL water with ultrasonic for 5 min, and then 0.50 mL 1-octano was added followed by vigorous mixing. Aliquots (in triplicate) from each organic and aqueous layer (50 μL) were carefully withdrawn with pipette and transferred into 96-well plate, respectively. The UV absorption value of individual well from the well plate was measured using a microplate reader (PerkinElmer, Waltham, MA, United States) at 245 nm. Log *P* value was calculated using the equation: log ([UV value in 1-octanol]/[UV value in water]) to access partition coefficient. Solvent corrected normalized UV values were first used to calculate log *P* value. Values for calculated log *P* (Clog *P*) were obtained with ChemBioDraw Ultra 14.0 software.

Saturation solubilities of FTS and FTS-IR783 were determined in distilled water. Excess amount of FTS and FTS-IR783 was added to 100 mL distilled water and shocked for 30 min at 25 °C, respectively. After centrifuged at 12,000 r/min for 15 min, drug concentrations were determined by measuring the UV absorbance at 245 nm, in each case the solubility determination was peformed in replicate for three times.

Fluorescence emission spectra of FTS-IR783

Fluorescence emission spectra were obtained with a RF-6000 spectrofluorometer (Shimazu, Japan) with the excitation wavelength (700 nm) and emission wavelength (720–900 nm). The concentration dependent (0.22, 0.88, 3.52, 14.06, 56.25, and 225.00 μM) fluorescence intensities were recorded for FTS-IR783. The fluorescence intensities were normalized and plotted with Origin software.

In vivo fluorescence imaging and biodistribution of FTS-IR783

All the fluorescence images were captured using IVIS whole-body imaging system (Perkin Elmer, Waltham, Massachusetts, USA) with an excitation wavelength at 640 nm and an long pass emission wavelength of 845 nm. For comparison of drug fluorescence, the female Balb\c-nude mice were imaged immediately after injected intraperitoneally (i.p.) with FTS, IR783, FTS-IR783 ($25\ mg \cdot kg^{-1}$) or vehicle individually. All drugs were dissolved in DMSO, respectively, and then prepared thoroughly according to the formula: 5% DMSO, 40% PEG400, 5% Tween 80, and 50% saline water.

For tissue imaging, the female Balb\c mice bearing 4T1-luc2 tumors were injected intraperitoneally (i.p.) with FTS-IR783 and sacrificed at 0, 1, 6, 24, 72, and 144 h post-injection, and the tumor, brain, heart, liver, spleen, thymus, lung, and kidney were isolated, rinsed with double distilled water and gently spread on black plate, then the real-time distributions of FTS-IR783 in isolated tissues were carried out immediately. The intensities of fluorescence signal were measured by drawing the ROIs on each organ and normalized to tumor volumes using Living Image software. For whole-body imaging, the female Balb\c-nude mice bearing MDA-MB-231 tumors were injected intravenously (i.v.) or intraperitoneally (i.p.) with FTS-IR783. Here, FTS-IR783 was dissolved in DMSO, and then prepared with saline water. The real-time distributions of FTS-IR783 in whole-body or tumors in living mice were carried out at 1, 6, 24, 72, and 144 h post-injection. The intensities of fluorescence signal were measured by drawing the ROIs on whole-body or tumors and normalized by subtracting the background ROIs recorded from the other mice without FTS-IR783 injection using Living Image software.

The pharmacokinetics of FTS and FTS-IR783

To compare the pharmacokinetics of FTS and FTS-IR783, Balb/c mice were intragastrically treated with 28 mM of FTS and FTS-IR783 (100 μL per 10 g). Tail vein blood (40 μL) was collected into heparin-treated tubes at 5, 10, 20, 30, 50, 80, 120, 240, 360, 480, 720, 1440, 1800, 2160, 2880, 4320 min. After centrifuged at 8000 r/min for 10 min, the plasma samples were harvested, and stored at −80 °C. Plasma samples (10 μL) were treated with acetonitrile containing internal standard (Liquiritin). Following centrifugation, the concentration of FTS or FTS-IR783 in the plasma was quantified by LC-MS/MS. The chromatograph conditions were set as follows: column, ACQUITY UPLC@ HSS T3 (2.1 × 100 mm, 1.8 μm); mobile phase A (0.01% formic acid), mobile phase B, (100% acetonitrile); gradient elution, 7 min; flow rate, $0.3\ mL \cdot min^{-1}$ and injection volume, 5 μL. The mass conditions were as follows: capillary voltage 3.5 kV, nozzle voltage 0.5 kV, sheath gas temperature 380 °C and gas temperature 300 °C with sheath gas flow of $11\ L \cdot min^{-1}$ and gas flow of $5\ L \cdot min^{-1}$. Electrospray ionization was performed in negative mode. The pharmacokinetic parameters of FTS and FTS-IR783 were calculated using WinNonlin software and shown in Supplementary Table 1.

The plasma protein binding rate of FTS-IR783

The plasma protein binding rate of FTS-IR783 was explored using equilibrium dialysis and LC-MS/MS. Blank plasma (2 mL) was put in dialysis bags, and then the bags were incubated in 10 mL isotonic sodium phosphate buffer (pH = 7.4) containing 2.5, 5, and 10 μM of FTS-IR783, respectively, for 24 h at 4 °C. Dialysis bag with very high permeability and a molecular weight cut-off of 7000 Da were used. After dialysis was completed, 200 μL of the resulting plasma and buffer dialysates was recovered and analyzed by LC–MS/MS after sample preparation. The plasma protein binding rate of FTS-IR783 was shown in Supplementary Table 2.

In vivo tumor models

Tumor in-situ mice model. 4T1-luc2 cells (50,000 cells per mouse) were suspended in 50 μL of PBS buffer/Matrigel (BD Pharmingen, USA) mixed solution (2:1, *v*/*v*) and subcutaneously inoculated into the fourth mammary fat pad of Balb/c mice on the right side. After 3 days for rest, the mice were randomized into five groups ($n = 6$) and injected intraperitoneally for 14 days as following: model (vehicle), FTS ($10\ mg \cdot kg^{-1}$), paclitaxel (PTX, $10\ mg \cdot kg^{-1}$), low dose of FTS-IR783 ($15\ mg \cdot kg^{-1}$) and high dose of FTS-IR783 ($30\ mg \cdot kg^{-1}$). The tumor volume and body weights of the mice were recorded every 3 days. The whole-body images were captured every week. Finally, the mice were sacrificed, and organs (including liver, kidney, heart, spleen, and lung) of each mouse were excised and weighed. The tumor volume and tumor weight were measured. Tumor volume (TV), defined based on two dimensions (L, long diameter; W, wide diameter), was measured by calipers, and calculated as formula: $TV\ (mm^3) = (L \times W^2)/2$.

Tumor metastasis model. 4T1-luc2 cells (10,000 cells per mouse) were suspended in 100 μL of PBS buffer and injected by tail vein. After 2 days for rest, mice were randomized into five groups ($n = 6$) and intraperitoneally administered with vehicle (model), $10\ mg \cdot kg^{-1}$ of FTS, $10\ mg \cdot kg^{-1}$ of PTX, $15\ mg \cdot kg^{-1}$ of FTS-IR783 and $30\ mg \cdot kg^{-1}$ of FTS-IR783 for 18 days, respectively. The whole-body images were captured at day 0 and day 20. The body weights of mice were measured every 3 days. Finally, the mice were sacrificed, and organs (including liver, kidney, heart, spleen, and lung) of each mouse were excised and weighed. The tumor numbers of lung tissues were measured.

Hematoxylin and eosin (H&E) staining

Lung, liver, spleen, and kidney tissue specimens were fixed, paraffin-embedded, and sliced up (4 μm). Then, slices were stained by hematoxylin for 30 s and 0.5% eosin for 10 s, covered with neutral gum, and examined using a light microscope (Leica DM750, Wetzlar, GER).

MTT assay

The cells were treated with drugs (0, 2, 4, 6, 8, 10, 25, 50, and 70 μM) or vehicle for 48 h, cultured with MTT solution (0.5 mg · mL^{-1}) at 37 °C for 4–6 h, and then dissolved by DMSO. The absorbance values were measured using a microplate reader (PerkinElmer, Waltham, MA, United States) at 490 nm. The IC_{50} values of drugs were calculated using the GraphPad Prism 5 software for each cell line and shown in Supplementary Table 3.

Cell proliferation assays

For 5-ethynyl-29-deoxyuridine (EdU) assay: after treatments with FTS-IR783, FTS or vehicle for 48 h, the cells were incubated with EdU labeling medium (50 μM) at 37 °C for 2 h before fixation. Detection of incorporated EdU was achieved with the Cell-Light EdU Apollo 488 In Vitro Imaging Kit (RiboBio, China), according to the manufacturer's protocol. For colony formation assay: cells were seeded in six-well plates (200 cells per well), then treated with FTS-IR783, FTS or vehicle for 10–14 days to allow the formation of colonies, during the period the medium was changed every other day. After the treatments, the cells were fixed with methanol for 15 min, followed by Giemsa staining for another 30 min. The stained colonies were counted on microscope, and the colony formation rate was calculated as percentage of the control group.

Wound healing assay

Wounds were created on a monolayer of cells at 95% confluence using a plastic pipette tip. The cells were treated with serum-free medium containing FTS-IR783, FTS, or vehicle. Images of wounds were photographed at 0, 24, and 48 h after drug treatments using a microscope (Leica, GER) at ×10 magnification.

Western blotting

After treated with FTS-IR783, FTS, or vehicle for 48 h, the cell extracts were prepared using RIPA lysis buffer, and quantified using Coomassie Brilliant Blue Kit (Bio-Rad, Hercules, CA, USA). Then, protein samples were separated by SDS-PAGE, transferred to PVDF membrane, blocked with 5% BSA and incubated with primary antibodies overnight at 4 °C. ECL chemiluminescence reagent was applied to detect fluorescent signals using Fluor Chem E (Santa Clara, CA, USA).

Flow cytometry analysis for Ki67 expression

After treated with FTS-IR783, FTS, or vehicle for 48 h, the cells were then fixed, incubated with 0.5% Triton™ X-100, blocked with 5% BSA. After incubated with primary antibody Ki67 (Alexa Flour 488) (1:50) at room temperature for 1 h, the cells were analyzed on a BD FACScalibur flow cytometer (BD bioscience, San Jose, CA), and the fluorescence of cells was calculated using FlowJo7.6 software.

FTS-IR783 uptake detection in vitro

For live-cell real-time fluorescence detection: cells were seeded into confocal dish (5000 cells per well) and cultured overnight. The real-time fluorescence of cells was detected at 5 min, 1, 2, and 3 h with a continuous administration of FTS-IR783 (50 μM) for 3 h in a stable humidified atmosphere with 5% CO_2 at 37 °C using Leica TCS SP8 confocal microscope (Leica, GER). For confocal imaging: the cells were treated with FTS-IR783 (50 μM) for 1 h, fixed, incubated with DAPI (5 μg· mL^{-1}), captured using Leica TCS SP8 confocal microscope (Leica, GER) and analyzed using Image J software. For flow cytometer analysis: the cells were treated with FTS-IR783 (5 μM) for 1 h, and analyzed on a BD FACScalibur flow cytometer (BD bioscience, San Jose, CA).

Real-time quantitative polymerase chain reaction (PCR) analysis

MDA-MB-231, BT-549, SK-BR-3, BT-474, and MCF-7 cells were harvested under normal culture. Total mRNA was isolated using TRIzol reagent (Invitrogen, United States) and reverse-transcripted into cDNA following the Prime Script™ RT reagent Kit (TaKaRa, Shiga, Japan). SYBR Green real-time PCR amplification and detection were then performed using an ABI 7500 system (Applied Biosystems, Foster City, CA, United States). Relative gene expression was normalized to GAPDH. Sequences of PCR primers were shown in Supplementary Table 4.

Absorption-inhibition test

After 1 h of serum-free MEM medium incubation, the MDA-MB-231 cells were pretreated with OATP inhibitors (BSP, 250 μM; CCK8, 20 μM; E2G, 10 μM) or endocytosis inhibitors (Sucrose, 450 μM; Chlorpromazine, 10 μg · mL^{-1}; Amiloride, 50 μM; Methyl-β-cyclodextrin, 10 μM) for 1 h. Then, the cells were incubated with FTS-IR783 (5 μM) for 0, 5, 15, 45, or 90 min and analyzed on a BD FACScalibur flow cytometer (BD bioscience, San Jose, CA), and the fluorescence of cells was calculated using FlowJo7.6 software.

Subcellular distribution of FTS-IR783 in live cells

For single cell sequence scanning: MDA-MB-231 cells treated with FTS-IR783 (50 μM) at 37 °C for 3 h, the single cell was scanned for 20 sequences using a Leica TCS SP8 confocal microscope (Leica, GER). For organelle imaging: cells were treated with FTS-IR783 (50 μM) for 1 h, incubated with dyes (mitochondria (400 nM), endoplasmic reticulum (1 μM), lysosome (50 nM), or Golgi apparatus dye (2 μL for 10,000 cells), respectively), fixed, and incubated with DAPI (5 μg · mL^{-1}). The images were captured using a confocal microscope. The correlation analysis between fluorescence values of FTS-IR783 and organelles was calculated by linear regression using GraphPad.

Pull-down assay and analysis

Sepharose 4B beads were activated and suspended in the coupling solution containing FTS, IR783, FTS-IR783 (each of 100 μM) or DMSO as a control at 4 °C overnight. The Sepharose 4B beads of each group were incubated with the lysate of MDA-MB-231 cells in reaction buffer at 4 °C overnight, then separated in SDS-PAGE and indentified by LC-MS/MS. The LC/MS/MS analysis was conducted by PTM Biolabs Inc. (Hangzhou, China). The resulting MS/MS data were processed using Proteome Discoverer 1.3. Tandem mass spectra were searched against SwissProt Human (20422 sequence) database. The identified proteins in each group were analyzed using Venny 2.1 and the identified 331 FTS-IR783 specific-binding proteins were listed in Supplementary Table 5. KEGG pathway enrichment analysis was performed for the identified 331 FTS-IR783 specific-binding proteins using the online tool Database for Annotation, Visualization and Integrated Discovery (DAVID) Bioinformatics Resources 6.8 (https://david.ncifcrf.gov/tools.jsp) and the online software Omicshare. The top 10 KEGG pathways with $P < 0.01$ were selected.

Molecular docking

The docking study was performed by AutoDockVina software. The 3D structures of AMPK (PDB ID: 4CFF) were downloaded from PDB database, ligand was removed via Chimera and prepared in ADT for docking. FTS-IR783 structure was converted to 3D coordinates by ChemDraw 12.0. The size of space was set as 45 × 45 × 45 point and other parameter was performed with default of the docking software. Lamarckian genetic algorithm was used for 50 runs. The docking result was viewed by Chimera software.

Cell thermal shift assay (CETSA)

The potential interaction between FTS-IR783, FTS, and target proteins were assessed by CETSA as previously described [21, 22]. Briefly, the lysate of MDA-MB-231 cells were incubated with FTS-IR783, FTS, or DMSO (as vehicle) for 30 min at room temperature, respectively. Then, each of the resulted aliquots was divided into six smaller parts and heated at indicated temperatures (37, 41, 45,

49, 53, and 57 °C) for 7 min. After centrifuged, the soluble fractions were analyzed by Western blotting.

Immunohistochemistry (IHC)
Tumor tissues were fixed, paraffin-embedded, and sliced up (4 μm). The deparaffinized and rehydrated slices were incubated with natrium citric (0.01 M) for antigen retrieval and with diluted anti-p-AMPKα overnight at 4 °C in turn. Following procedures were performed using the immunostaining kit (BOSTER Biological Technology) based on the manufacturer's instructions.

Statistics
Data were presented as mean ± SD. Student's *t*-test was used for determining significance of intergroup data, while the significance of multiple comparisons was assessed by one-way ANOVA. Statistical analyses were carried out using Graph Pad Prism 7.0c Software. A $P < 0.05$ was considered statistically significant.

RESULTS

IR783 conjugation with FTS improved the hydrophilicity, fluorescence imaging capability of FTS
FTS was conjugated with IR783 to yield compound 4 according to the synthesis scheme shown in Fig. 1a. The ^{13}C- and ^{1}H- NMR data were in agreement with the desired structure of Compound 4 (Supplementary Fig. 1a, b). The ^{13}C-^{1}H COSY and ^{1}H-^{1}H COSY data were in accordance with the results obtained for the ^{13}C- and ^{1}H-NMR spectra, further confirming that compound 4 was the target product (Supplementary Fig. 1c, d). The FT-IR spectrum showed transmittance bands for compound 4, including the characteristic bands at 3431.5 cm^{-1} (N-H stretching vibration), 1111.3 and 1169.6 cm^{-1} (S–O stretching vibration), 3049.9 cm^{-1} (C=C–H stretching vibration) and 1741.9 cm^{-1} (C=O stretching vibration) [23], which were in agreement with the desired structure (Supplementary Fig. 1e). The chemical composition of compound 4 was confirmed by mass spectrometry ([M + H] + *m/z* 1108.5031 for $C_{62}H_{81}N_3O_7S_4$ (calcd. 1108.503)) (Supplementary Fig. 1f).

The log *P* value ($C_{octanol}/C_{water}$) is a well-established measure of the hydrophilicity of a compound [24]. The log *P* values of FTS and compound 4 are 6.393 (cal. 7.572) and 0.384 (cal. 1.752), respectively (Fig. 1b). The water solubility of compound 4 was significantly increased (Fig. 1c). Importantly, the solubility of FTS-IR783 in water was amplified up to 186 μg · mL^{-1} compared to FTS (2 μg · mL^{-1}), reflecting a highest solubility increase of 93 times (Fig. 1d). In addition, the fluorescence analysis results indicated that the emission maximum of compound 4 occurred at ~800 nm (Fig. 1e), which was similar to that of the NIRF dye IR783 [17]. Red fluorescence was observed in mice after intraperitoneal injection with IR783 and compound 4 (Fig. 1f).

The pharmacokinetic profiles (plasma concentrations versus time) after single oral administration of 28 mM FTS and FTS-IR783 in the two treatment groups were presented in Supplementary Fig. 1g, h and Supplementary Table 1. The plasma concentration of FTS was decreased rapidly from 80 to 240 min (Supplementary Fig. 1g), while the plasma concentration of FTS-IR783 changed slowly (Supplementary Fig. 1h). Compared with FTS, although the C_{max} of FTS-IR783 was decreased (from 18.72 ± 6.17 μM to 4.93 ± 0.10 μM), the $t_{1/2}$, AUC_{0-t}, $AUC_{0-\infty}$, V_d and MRT_{0-t} of FTS-IR783 were both significantly increased. The longer retention time made the relative bioavailability of FTS-IR783 increase by 90.7% compared with FTS. Also, the plasma protein binding rate of FTS-IR783 was explored using equilibrium dialysis and LC-MS/MS. The results showed that there was no significant difference in plasma protein binding rate among each concentration. The plasma protein binding rate of FTS-IR783 was about 55.39% ± 1.27% (Supplementary Table 2).

The FTS-IR783 conjugate showed strong tumor-targeting ability in vivo
The isolated tissues images from 4T1-luc2 tumor-bearing BALB\c mice (Fig. 1g) showed that FTS-IR783 was mainly distributed in liver, thymus, and tumor after intraperitoneal injection. The fluorescence gradually accumulated in tumors starting at 6 h and peaking at 24 h post-injection. Even at 144 h post-injection, fluorescence signals in tumor could also be clearly observed while almost being cleared away from normal tissues. At the same time, MDA-MB-231 tumor-bearing BALB/c-nude mice injected intraperitoneally with FTS-IR783 showed similar results. Differently, images of MDA-MB-231 tumor-bearing BALB/c-nude mice injected intravenously with FTS-IR783 showed that the fluorescence signals were observed in almost the entire body of the mice after injection, and then cleared away from the body. However, the drug clearance was significantly slower in the tumor than in other tissues (Fig. 1h). These results indicated the significant tumor-targeting capability of the FTS-IR783 conjugate in vivo.

FTS-IR783 showed stronger anti-cancer therapeutic efficacy than FTS both in vivo and in vitro
The cancer therapeutic efficacy of FTS-IR783 was assessed using two in vivo 4T1-luc2 tumor models (Supplementary Fig. 2a, b). The results showed that FTS, FTS-IR783, and PTX could inhibit tumor growth to different degrees. Compared with that in the model group, as the tumors grew, the luminescent intensity was inhibited over time both visually and quantitatively in the drug treatment groups (Fig. 2a, b). Consistently, the tumor volume and tumor weight were markedly decreased (Fig. 2c, d). By comparison with the model group, the tumor inhibition rates of FTS, FTS-IR783 (15 and 30 mg · kg^{-1}) and PTX groups were determined to be 34.32% ± 33.96%, 35.21% ± 24.14%, 62.34 %± 27.74%, and 69.31% ± 20.96%, respectively. The in vitro anti-breast cancer effects of FTS-IR783 were also assessed. The MTT assay results showed that breast cancer cells were more sensitive to FTS-IR783 than FTS, however, the normal cells MCF10A was opposite (Fig. 2e and Supplementary Fig. 2c). The IC_{50} values were shown in Supplementary Table 3. Considering the diverse levels of FTS-IR783 and FTS sensitivity observed in these cells, MDA-MB-231 and 4T1-luc2 cells were chosen for further studies. EdU assays and cell colony assays were employed to explore the effects of FTS-IR783 on cell growth. In MDA-MB-231 cells, the number of EdU-positive cells was reduced by 74.35% ± 4.06% and 76.27% ± 7.16% after high-dose FTS-IR783 (4 μM) and FTS (10 μM) treatments, respectively, compared with that in control cells. Similarly, the number of EdU-positive 4T1-luc2 cells was reduced by 64.91% ± 3.86% (16 μM FTS-IR783) and 49.73% ± 6.02% (25 μM FTS) (Fig. 2f and Supplementary Fig. 2d). In addition, FTS-IR783 significantly reduced the colony number in breast cancer cells. The colony inhibition rates were 34.59% ± 1.50% and 86.51% ± 2.08%, respectively, after treatment with 4 μM FTS-IR783 in MDA-MB-231 cells and treatment with 16 μM FTS-IR783 in 4T1-luc2 cells. The colony inhibition rates of FTS were 37.09% ± 1.57% (10 μM) and 17.99% ± 6.23% (25 μM) in MDA-MB-231 and 4T1-luc2 cells, respectively (Supplementary Fig. 2e). In summary, FTS-IR783 showed stronger anti-growth effects than FTS at an equal dose. In addition, we determined the expressions of PCNA and Ki67 (two potential markers of cell proliferation) [25]. After the FTS-IR783 and FTS treatments, PCNA and Ki67 expressions were significantly decreased in both breast cancer cell lines (Fig. 2g, h).

The effect of FTS-IR783 on cancer metastasis was also evaluated. FTS-IR783 treatment (especially 30 mg · kg^{-1}) obviously decreased the luminescent intensity both visually and quantitatively compared with that in the model group (Fig. 2I, j). The number and size of metastatic tumors were significantly suppressed by FTS-IR783 (Fig. 2k, l). Compared with that in the model group, the average number of tumors in the FTS-, FTS-IR783- (15 and 30 mg · kg^{-1}) and PTX-treated groups were remarkably reduced

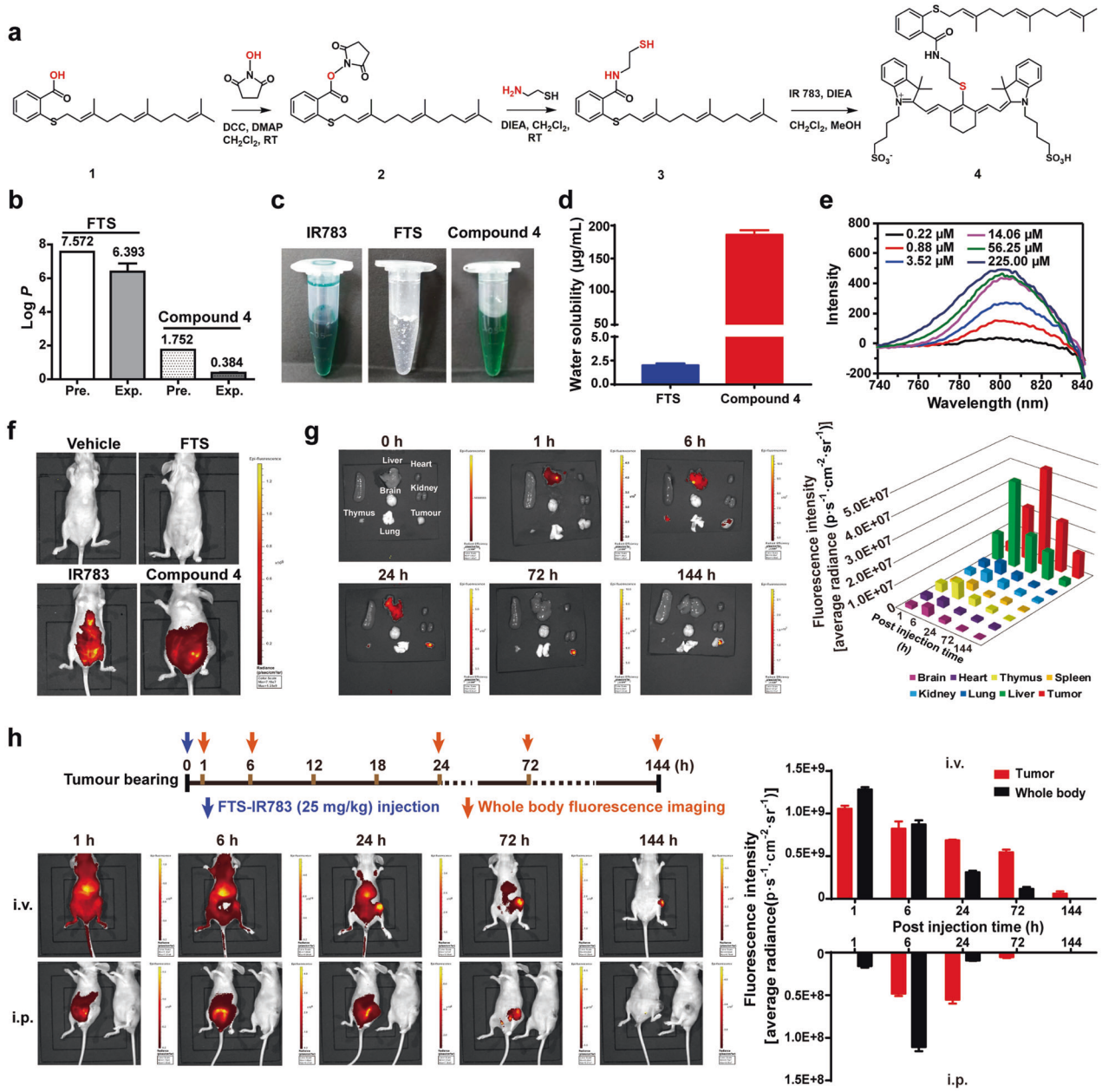

Fig. 1 Synthesis, characteristic and tumor-targeting evaluation of FTS-IR783 conjugate. a The synthesis scheme of FTS-IR783 conjugate. **b** Partition coefficients of FTS and FTS-IR783 conjugate were predicted using ChemBioDraw Ultra 14.0 software and detected using 1-octanol/Water assay. **c** Photographs of IR783, FTS, or FTS-IR783 aqueous solution (2.00 μM). **d** Water solubility of FTS and FTS-IR783 were detected using a microplate reader at 245 nm. Data are represented as mean ± S.D. **e** Concentration dependent fluorescence emission spectra of FTS-IR783 (0.22, 0.88, 3.52, 14.06, 56.25, and 225.00 μM) were detected using a RF-6000 spectrofluorometer with the excitation wavelength (700 nm) and emission wavelength (720–900 nm). **f** In vivo imaging abilities of FTS, IR783 and FTS-IR783 were assessed respectively in Balb/c-nude mice using a IVIS whole-body imaging system with an excitation at 640 nm and an long pass emission at 845 nm after a single intraperitoneal injection (25 mg · kg^{-1}). **g**, Representative fluorescent images of tissues isolated from 4T1-luc2 tumor-bearing Balb/c mice at 0, 1, 6, 24, 72, and 144 h after a single intraperitoneal injection of FTS-IR783 (25 mg · kg^{-1}) and the intensities of fluorescence signal of tissues were measured by drawing the ROIs using Living Image software. **h** Representative fluorescent images of MDA-MB-231 tumor-bearing Balb/c-nude mice at 1, 6, 24, 72, and 144 h after a single intravenous (i.v) or a single intraperitoneal (i.p.) injection of FTS-IR783 (25 mg · kg^{-1}), and the intensities of fluorescence signal of whole body of mice and tumors were measured by drawing the ROIs using Living Image software.

by 31.58% ± 24.46%, 30.70% ± 19.81%, 45.61% ± 19.31% and 58.77% ± 15.04%, respectively. The effect of FTS-IR783 on cell migration was also determined. A high dose of FTS-IR783 inhibited cell migration rates by 64.00% ± 5.66% and 80.51% ± 0.86%, respectively, in MDA-MB-231 and 4T1-luc2 cells. As expected, 10 and 25 μM FTS reduced cell migration rates by 47.43% ± 6.46% and 42.16% ± 5.05%, respectively, in MDA-MB-231 and 4T1-luc2 cells and exhibited weaker anti-migration ability than FTS-IR783 (Fig. 2m). The EMT-related markers [26] N-cadherin and vimentin protein levels were significantly reduced by FTS-IR783 and FTS, whereas the levels of E-cadherin were increased in both 4T1-luc2 and MDA-MB-231 cells (Fig. 2n).

In addition, FTS and PTX treatments caused weight loss in mice, while no significant alterations of the average body weight were observed for FTS-IR783 treatments in animal model (Supplementary Fig. 2f). Meanwhile, FTS-IR783 did not remarkably alter the

organ indexes (Supplementary Fig. 2g) and the structures of the liver, kidney and spleen (Supplementary Fig. 2h), demonstrating the low systemic toxicity of FTS-IR783 in vivo.

OATPs and endocytosis inhibitors decreased the uptake of FTS-IR783 in MDA-MB-231 breast cancer cells

The confocal results showed that an ~5–6-fold increase in the red fluorescent intensity was detected in MCF-7, MDA-MB-231, and 4T1-luc2 breast cancer cells compared to that in MCF10A cells (Fig. 3a). The flow cytometry results also showed that the fluorescence signals in breast cancer cell lines were ~1.5–3 times higher than those in MCF10A cells (Fig. 3b), further demonstrating that FTS-IR783 showed strong specific targeting of breast cancer cells in vitro.

Live-cell real-time fluorescence detection was used to monitor the accumulation of FTS-IR783 in MDA-MB-231 breast cancer cells. Parallel comparisons were performed that the uptake of FTS-IR783 in MDA-MB-231 cells gradually increased with time (Supplementary Fig. 3a). OATPs, which are a group of membrane-binding solute carriers, play a key role in the uptake of dyes such as IR783 by tumor cells [27]. We found that triple-negative breast cancer MDA-MB-231 and BT-549 cells show a higher expression level of OATPs than other breast cancer cells (Supplementary Fig. 3b). Considering the high sensitivity of FTS-IR783 in MDA-MB-231 cells (Fig. 2e), we chose to use MDA-MB-231 cells for further research on the tumor-targeting mechanism of FTS-IR783. After the nonselective OATP inhibitor BSP treatment, the fluorescent value of the cells was significantly decreased compared with that of cells treated with FTS-IR783 alone (Fig. 3c). Additionally, the OATP1B1 and OATP1B3 selective inhibitors estradiol-17β-glucuronide (E2G) and sincalide (CCK8) [28] markedly decreased the fluorescence signal of FTS-IR783 in cells compared with that in cells treated with FTS-IR783 alone, and CCK8 had a stronger effect (Fig. 3d, e and Supplementary Fig. 3c). These results demonstrated that OATPs played an important role in FTS-IR783 uptake, especially OATP1B3.

Since OATP blockade could not completely stop the uptake of FTS-IR783, we further explored the underlying uptake mechanism of FTS-IR783 in cancer cells. The pull-down assay and LC-MS/MS results showed that 331 proteins (Fig. 3f and Supplementary Table 5) might bind to FTS-IR783 specifically, and ~16 proteins were related to the endocytosis process (Fig. 3g). The endocytosis-related proteins clathrin and caveolin-1 were also found to bind to FTS-IR783 (Supplementary Table 5). After the nonselective endocytic inhibitor sucrose treatment, the fluorescence values of cells were significantly decreased compared with those of cells treated with FTS-IR783 alone (Fig. 3h). Moreover, the selective inhibitors of clathrin-mediated and caveolin-mediated endocytosis chlorpromazine and methyl-β-cyclodextrin remarkably decreased the fluorescence values of the cells compared with those of cells receiving FTS-IR783 single treatment (Fig. 3l, j and Supplementary Fig. 3d). Conversely, the macropinocytosis inhibitor amiloride had no influence on FTS-IR783 uptake (Fig. 3k and Supplementary Fig. 3d).

Considering the apparent influence of OATPs or endocytosis on FTS-IR783 uptake, we further determined which one plays the predominant role in the uptake process of FTS-IR783. At 90 min after drug treatment, compared with that of cells receiving FTS-IR783 treatment alone, the inhibition rates of cells receiving sucrose or BSP treatment alone were 9.50% and 49.43%, respectively, while the inhibition rate of cells receiving BSP and sucrose combination treatment was 60.31% (Fig. 3l).

The subcellular distribution of FTS-IR783 in breast cancer cells

Five representative images from single-cell sequence scanning clearly showed that red fluorescence was found in the cytoplasm of cells but not in the nuclear area (Fig. 4a). Meanwhile, the red fluorescence signal (FTS-IR783) was separated from the blue fluorescence signal (nuclear) (Fig. 4b, c), and there was a negative correlation between red fluorescence and blue fluorescence (Fig. 4d), suggesting that FTS-IR783 was not entrapped in the nucleus. We also visualized the overlap of the red fluorescence of FTS-IR783 with the green fluorescence of the mitochondria, endoplasmic reticulum, lysosome, and Golgi apparatus to different degrees while separating the red fluorescence from blue fluorescence (Fig. 4e, f). Correlation analysis showed positive correlations between FTS-IR783 and the mitochondria, endoplasmic reticulum, lysosome, and Golgi apparatus and negative correlations between FTS-IR783 and the nucleus (Fig. 4g).

FTS-IR783 and FTS both suppressed breast cancer dependent on mTOR

The mTOR signaling pathway plays a key role in the occurrence and development of cancer, especially in tumor growth, migration, and angiogenesis [29]. FTS could inhibit mTOR independently of Ras inhibition [30]. As FTS-IR783 has good anti-proliferation and anti-migration capacity both in vivo and in vitro, we explored whether FTS-IR783 treatment directly acts on the mTOR signaling pathway. Considering that MDA-MB-231 cells are the most sensitive to FTS-IR783 and FTS (Fig. 5a), these cells were chosen for further research. Similar to FTS, FTS-IR783 significantly decreased p-mTOR (S2448), p-mTOR (S2481), and p-p70S6K expression levels (Fig. 5b). Meanwhile, FTS-IR783 treatments obviously inhibited tumor growth and significantly decreased p-mTOR (S2448) and p-mTOR (S2481) expression levels in vivo (Fig. 5c, d). The mTOR inhibitor KU-0063794 increased the inhibitory effects of FTS-IR783 on p-mTOR (S2448), p-mTOR (S2481), and p-p70S6K expressions and enhanced the inhibitory effects of FTS-IR783 on breast cancer cells (Fig. 5e, f). In contrast, the mTOR activator MHY1485 reversed the inhibitory effects of FTS-IR783 on the expressions of p-mTOR (S2448), p-mTOR (S2481), and p-p70S6K and on cell viabilities (Fig. 5g, h).

FTS has been reported to inhibit cell proliferation and metastasis through the Raf/MEK/ERK and PI3K/Akt/mTOR signaling pathways [8, 9]. We found that FTS treatment downregulated the expressions of Ras, p-Akt, and p-ERK. Conversely, FTS-IR783 treatments had no significant effects on Ras and p-Akt protein expressions but downregulated the expression of p-ERK (Fig. 5i), suggesting the different anticancer mechanism of FTS-IR783 compared to that of FTS.

FTS-IR783 regulated TSC2/mTOR signaling by directly binding with and activating AMPK

Ras, GSK3β, Akt, and AMPK are known to be upstream regulatory elements of mTOR signaling [31]. The pull-down results showed that FTS-IR783 exhibited good affinity toward the AMPK α and β subunits rather than Ras, GSK3β, Akt, and mTOR (Fig. 6a). Furthermore, FTS-IR783 was predicted to bind with the Thr26, Gly28, Ile46, Asn48, Thr85, and Asn110 residues of AMPK (binding energy: −7.7, Fig. 6b). The CETSA results reinforced our point that FTS-IR783 could shift the Tm_{50} values of AMPK α and β by 1.63 ± 0.80 °C and 1.56 ± 1.30 °C, respectively (Fig. 6c), whereas no affinity of FTS-IR783 was observed toward Ras, GSK3β, Akt, and mTOR (Fig. 6d). The increase in thermal stabilization suggested that FTS-IR783 could bind with AMPK directly. Conversely, FTS showed no affinity toward the AMPK α and β subunits in either the pull-down or CETSA assay data (Fig. 6e, f), indicating that after conjugation with IR783, the target of the FTS conjugate was changed.

Next, the effect of drugs on AMPK activation was measured. IHC results showed that FTS had no effect on in-situ expression of p-AMPKα. Conversely, FTS-IR783 significantly enhanced the phosphorylation levels of AMPKα (Fig. 6g), demonstrating that FTS-IR783 could directly bind with and activate AMPK. Despite dose-dependently enhancing the phosphorylation levels of the AMPK α and β subunits, FTS-IR783 subsequently phosphorylated TSC2 both in vitro and in vivo (Fig. 6h, i). Moreover, the AMPK inhibitor dorsomorphin reversed the inhibitory effect of FTS-IR783 on the

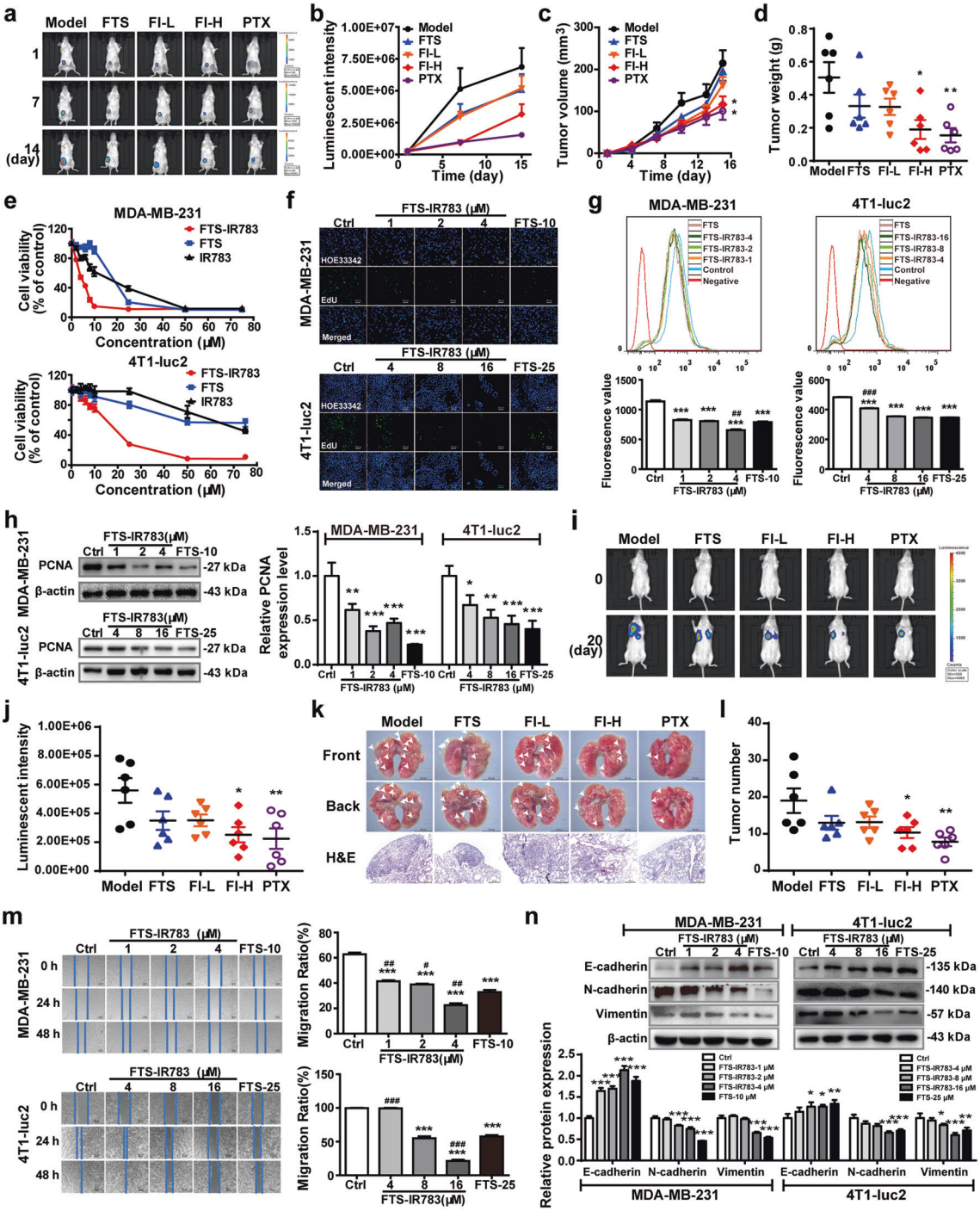

Fig. 2 FTS-IR783 showed stronger anti-cancer therapeutic efficacy than FTS both in vivo and in vitro. Representative bioluminescent images of tumor-bearing Balb/c mice (**a**) and tumor luminescent intensity (**b**) were captured and analyzed at day 1, 7, and 14 after treatments with vehicle, FTS (10 mg · kg^{-1}), paclitaxel (PTX, 10 mg · kg^{-1}), low dose of FTS-IR783 (FI-L, 15 mg · kg^{-1}) and high dose of FTS-IR783 (FI-H, 30 mg · kg^{-1}). **c** Tumor volumes of the mice were recorded every 3 days. **d** Tumor weight was recorded after isolated from sacrificed mice at the end ($n = 6$ each group). **e** Cell viabilities of MDA-MB-231 and 4T1-luc2 cells were detected after treated with FTS, IR783, FTS-IR783 (0, 2, 4, 6, 8, 10, 25, 50 and 70 μM) or vehicle for 48 h. **f** The anti-proliferation activity of FTS (10 μM for MDA-MB-231 and 25 μM for 4T1-luc2) and FTS-IR783 (1, 2, 4 μM for MDA-MB-231 and 4, 8, 16 μM for 4T1-luc2) were detected by EdU staining. Effects of FTS-IR783 and FTS on proliferation-associated proteins Ki67 (**g**) and PCNA (**h**) in MDA-MB-231 and 4T1-luc2 cells were measured using flow cytometry and Western blotting. Whole-body bioluminescent images of cancer metastasis Balb/c mice (**i**) and tumor luminescent intensity (**j**) were captured and analyzed at day 0 and 20 after treatments ($n = 6$ each group). **k** Lung tissues were captured and lung tissues pathologic changes were observed by H&E staining. **l** Numbers of metastatic lesions in lung were recorded**. m** The anti-migration activity of FTS and FTS-IR783 was detected using Wound healing assay. **n** Effects of FTS-IR783 and FTS on migration-associated proteins E-cadherin, N-cadherin, and vimentin were measured. $^{*}P < 0.05$, $^{**}P < 0.01$ and $^{***}P < 0.001$ vs. Model or Ctrl (control). $^{\#}P < 0.05$, $^{\#\#}P < 0.01$, and $^{\#\#\#}P < 0.001$ vs. FTS, by one-way ANOVA. Data were shown as Mean ± SD.

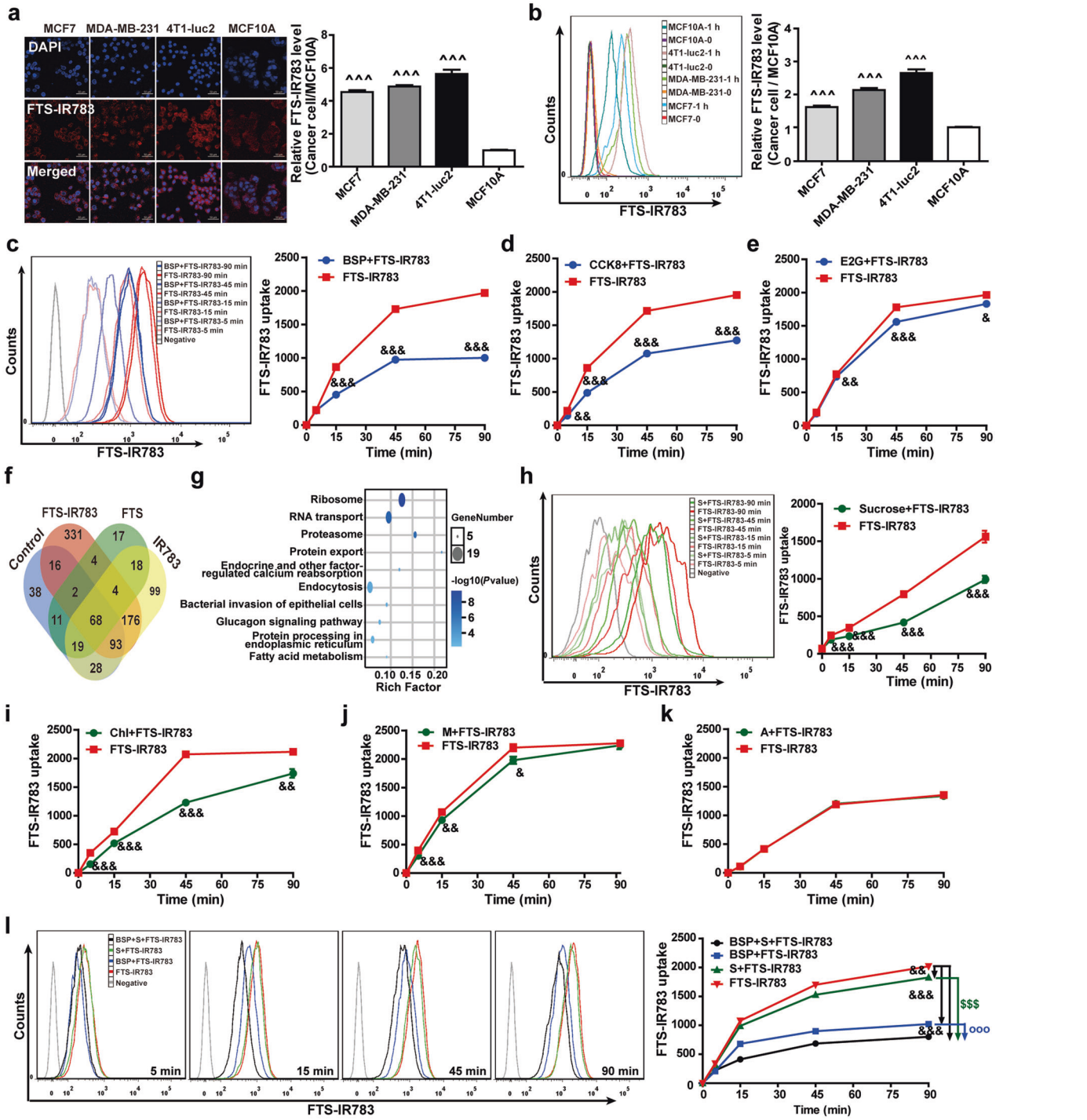

Fig. 3 The uptake mechanism of FTS-IR783 in MDA-MB-231 cells. The accumulation of FTS-IR783 in breast cancer cells MCF-7, MDA-MB-231, and 4T1-luc2, and normal cells MCF10A were detected after FTS-IR783 treatments for 1 h using confocal microscope (50 μM) (**a**) and flow cytometry (5 μM) (**b**). ^^^$P < 0.001$ vs. MCF10A, by one-way ANOVA. Effects of nonselective OATP inhibitor BSP (**c**), selective OATP1B3 inhibitor CCK8 (**d**), and selective OATP1B1 inhibitor E2G (**e**) on FTS-IR783 uptake in MDA-MB-231 cells at 0, 5, 15, 45, 90 min after inhibitor pretreatments for 1 h and FTS-IR783 (5 μM) treatments were assessed using flow cytometry. $^{\&}P < 0.05$, $^{\&\&}P < 0.01$ and $^{\&\&\&}P < 0.001$ vs. FTS-IR783, by two-tailed unpaired Student's *t*-test. **f** The numbers of identified pull-down proteins in each group were analyzed using Venny 2.1. **g** KEGG enrichment analysis of 331 proteins specifically pulled down by FTS-IR783 performed by DAVID and visualized by Omicshare. Effects of nonselective endocytosis inhibitor sucrose (**h**), clathrin-mediated selective inhibitors chlorpromazine (Chl) (**i**), caveolin-mediated selective inhibitors methyl-β-cyclodextrin (M) (**j**), and macropinocytosis inhibitor amiloride (A) (**k**) on FTS-IR783 uptake in MDA-MB-231 cells at 0, 5, 15, 45, 90 min after inhibitor pretreatments for 1 h and FTS-IR783 (5 μM) treatments. $^{\&}P < 0.05$, $^{\&\&}P < 0.01$ and $^{\&\&\&}P < 0.001$ vs. FTS-IR783, by two-tailed unpaired Student's *t*-test. **l** Effects of BSP and sucrose (S) combination on FTS-IR783 uptake in MDA-MB-231 cells at 0, 5, 15, 45, 90 min after inhibitor pretreatments for 1 h and FTS-IR783 (5 μM) treatments. $^{\&\&}P < 0.01$ and $^{\&\&\&}P < 0.001$ vs. FTS-IR783, $^{\$\$\$}P < 0.001$ vs. sucrose, $^{ooo}P < 0.001$ vs. BSP, by one-way ANOVA. The data were shown as Mean ± SD.

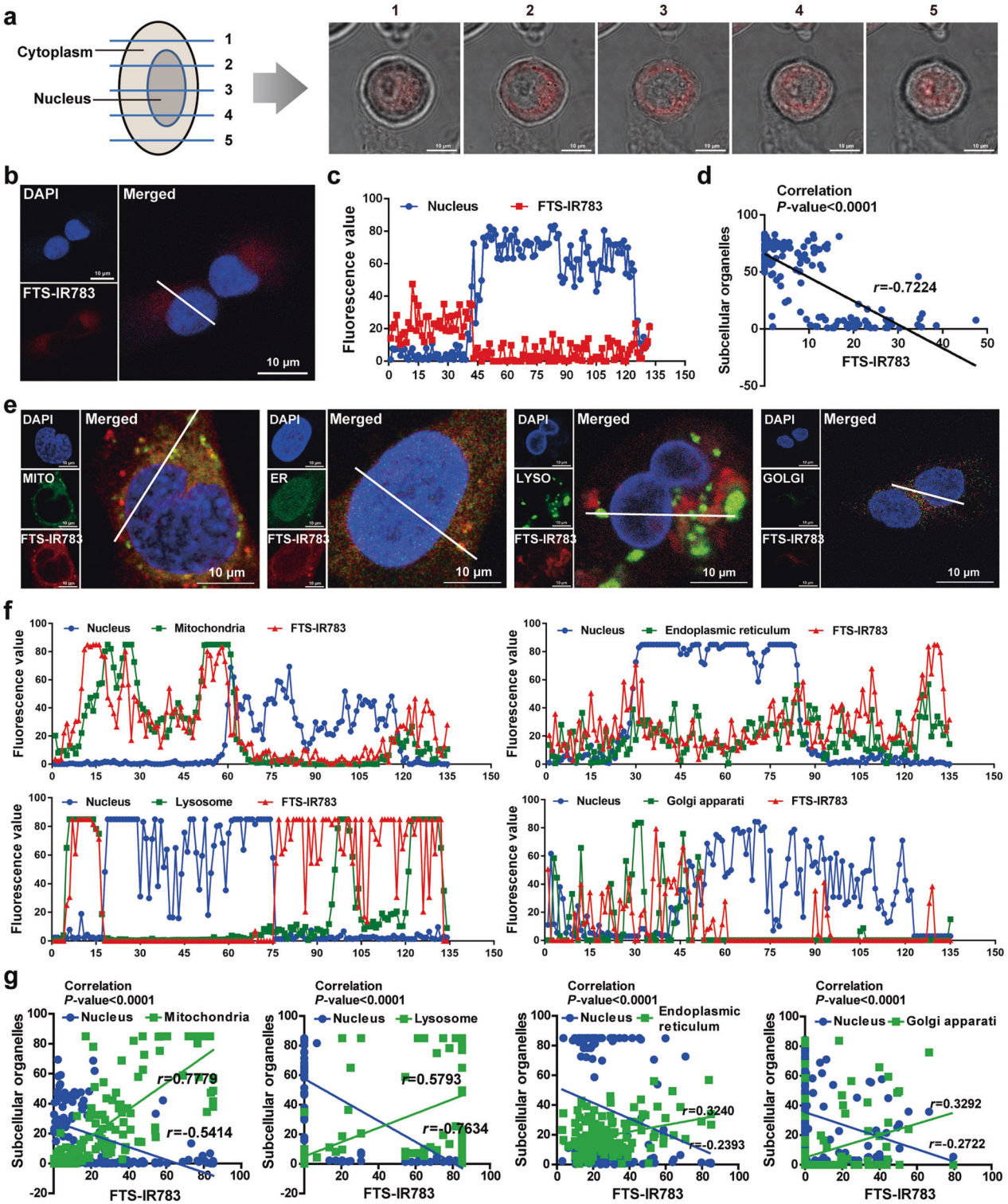

Fig. 4 **The subcellular distribution of FTS-IR783 in MDA-MB-231 cells. a** Representative sequence scanning images of MDA-MB-231 cells were captured using confocal microscope after treated with FTS-IR783 (50 μM) for 3 h. **b** Colocalization images of FTS-IR783 and nucleus (DAPI) captured using confocal microscope after treated with FTS-IR783 (50 μM) for 1 h. **c** Fluorescence curves of FTS-IR783 and nucleus were analyzed using Image J software. **d** The correlation analysis between fluorescence values of FTS-IR783 and nucleus was calculated by linear regression using GraphPad. **e** Colocalization images of FTS-IR783 and organelles including mitochondria (MITO), endoplasmic reticulum (ER), lysosome (LYSO), or Golgi apparatus (GOLGI) were captured after treated with FTS-IR783 (50 μM) for 1 h, then stained with mitochondria (400 nM), endoplasmic reticulum (1 μM), and lysosome (50 nM) for 30 min, and Golgi apparatus dye (2 μL for 10,000 cells) for 16 h, respectively. **f** Fluorescence curves of FTS-IR783 and organelles were analyzed using Image J software. **g** The correlation analysis between fluorescence values of FTS-IR783 and organelles were calculated by linear regression using GraphPad.

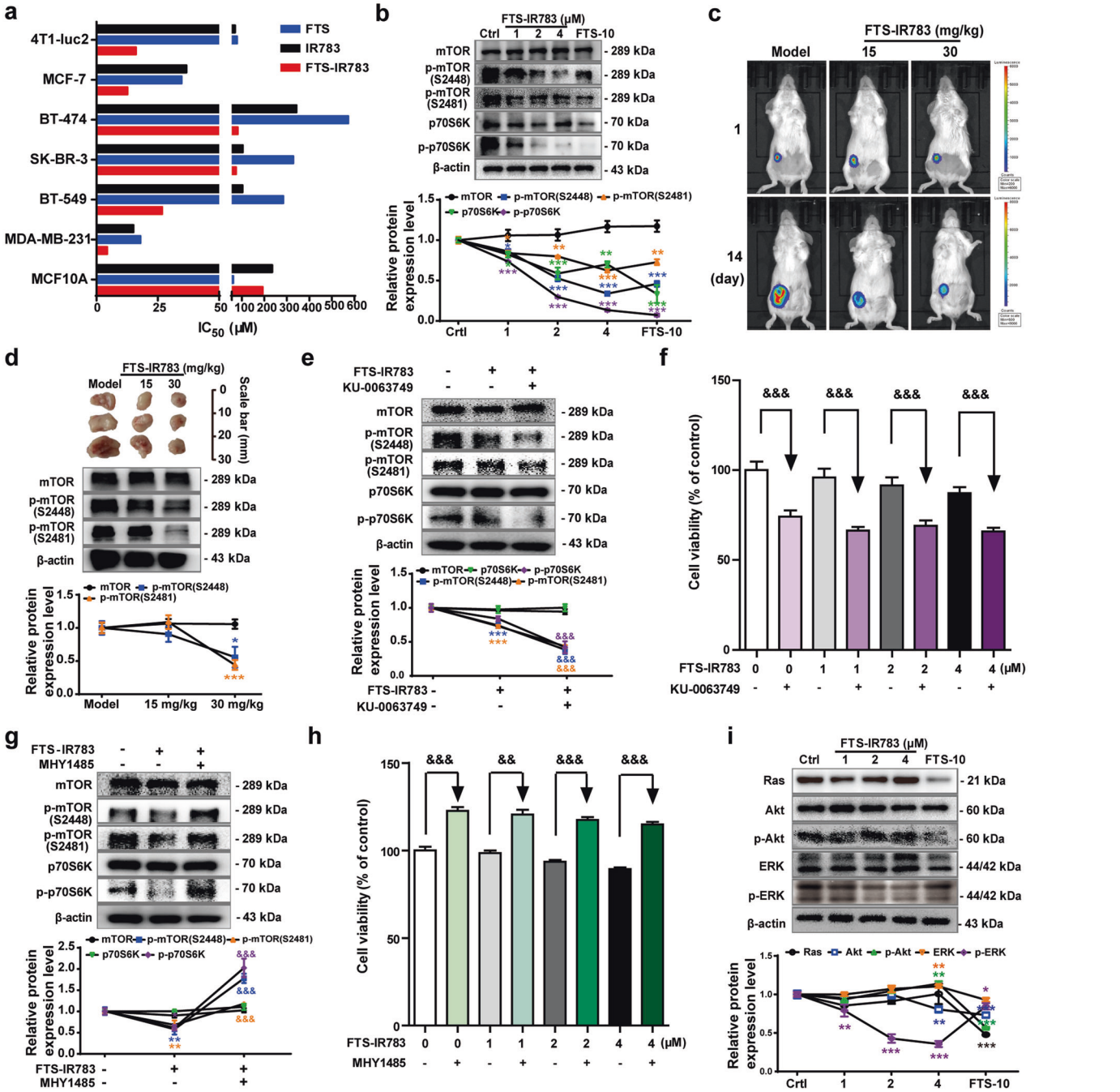

Fig. 5 FTS-IR783 mTOR-dependently suppressed breast cancer. a Comparition of IC_{50} values of FTS, IR783, and FTS-IR783 on MDA-MB-231, BT-549, SK-BR-3, BT-474, MCF-7, 4T1-luc2 and MCF10A cells after treated for 48 h. **b** The expressions of mTOR, p-mTOR2448, p-mTOR2481, p70S6K, p-p70S6K proteins in MDA-MB-231 cells were detected after treatments with FTS-IR783 (1, 2, 4 μM) and FTS (10 μM) for 48 h. **c** Representative whole-body bioluminescent images of 4T1-luc2 tumor-bearing Balb/c mice at day 1 and day 14 after FTS-IR783 treatments (15 and 30 mg · kg^{-1}). **d** Tumor images were taken and the protein expressions of mTOR, p-mTOR2448, and p-mTOR2481 were detected in tumor tissue by Western blotting. Effects of mTOR inhibitor KU-0063794 on mTOR, p-mTOR2448, p-mTOR2481, p70S6K and p-p70S6K proteins (**e**) and cell viability (**f**) in MDA-MB-231 cells were observed after KU-0063794 (50 nM) and FTS-IR783 (4 μM) treatments for 48 h. Effects of mTOR activator MHY1485 on mTOR, p-mTOR2448, p-mTOR2481, p70S6K, and p-p70S6K proteins (**g**) and cell viability (**h**) in MDA-MB-231 cells were investigated after MHY1485 (20 μM) and FTS-IR783 (4 μM) treatments for 48 h. **i** The protein expressions of Ras, Akt, p-Akt, ERK, and p-ERK in MDA-MB-231 cells were measured after FTS-IR783 (1, 2, 4 μM) and FTS (10 μM) treatments for 48 h. $^{*}P < 0.05$, $^{**}P < 0.01$ and $^{***}P < 0.001$ vs. Model or Ctrl (control), $^{\&\&}P < 0.01$, $^{\&\&\&}P < 0.001$ vs. FTS-IR783, by two-tailed unpaired Student's *t*-test. The data were shown as Mean ± SD.

viability of breast cancer cells in a dose-dependent manner (Fig. 6j). Additionally, the AMPK inhibitor dorsomorphin also reversed the activating effects of FTS-IR783 on the expressions of p-AMPKα and p-AMPKβ and the inhibitory effects of FTS-IR783 on the expressions of p-mTOR (S2448), p-mTOR (S2481), and p-p70S6K (Fig. 6k).

DISCUSSION

In this study, we successfully improved the hydrophilicity, tumor-targeting, and antitumor activity of FTS via conjugation with IR783. By systematically elucidating the underlying tumor-targeting and antitumor mechanisms of the new conjugate, we unexpectedly

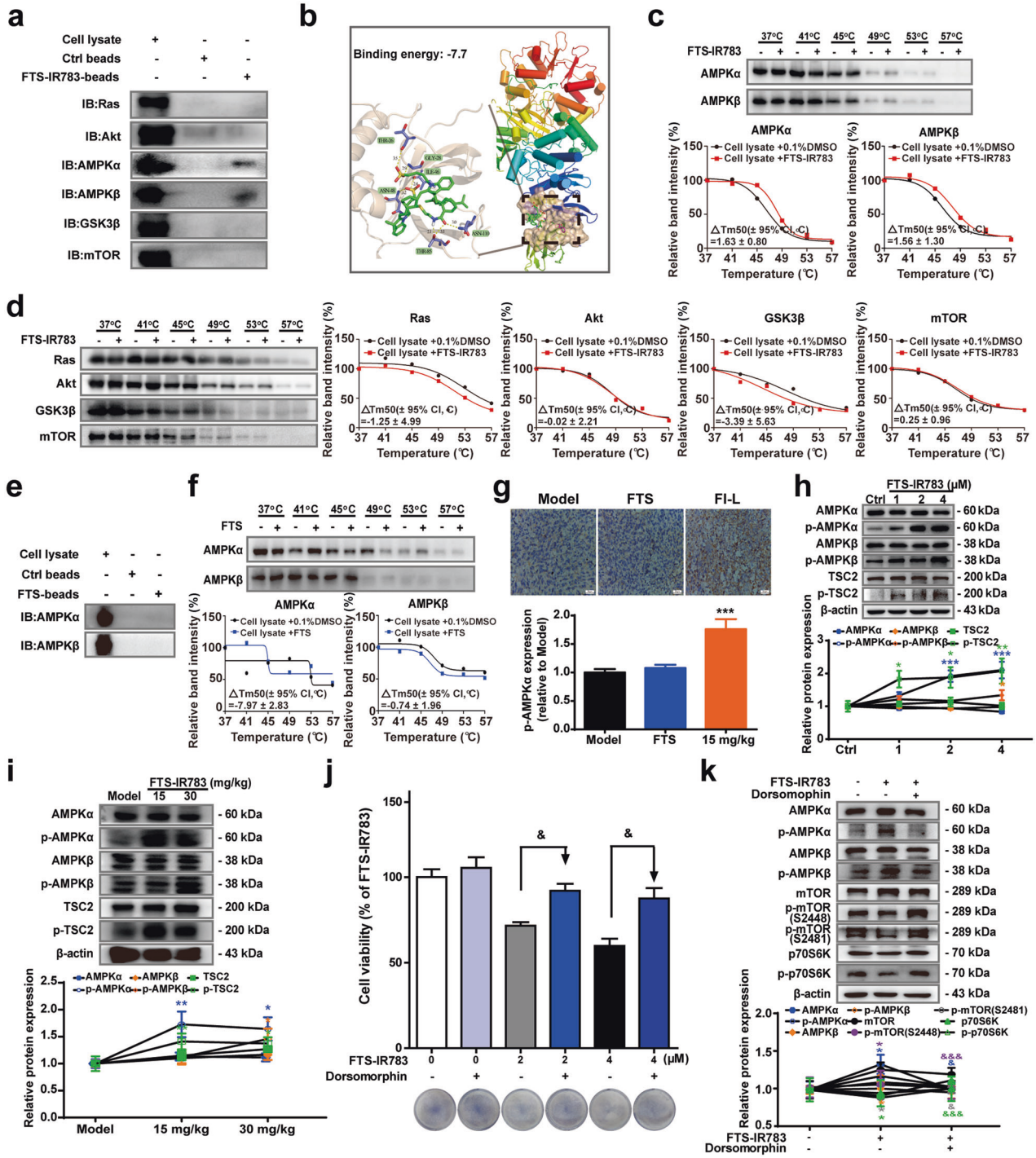

Fig. 6 FTS-IR783 directly bound with and activated AMPK and subsequently regulated TSC2/mTOR signaling pathway. a The affinities of FTS-IR783 and mTOR, Ras, Akt, AMPKα, AMPKβ, and GSK3β were detected by pull-down assay, respectively. **b** The binding of FTS-IR783 with AMPK was analyzed by molecular docking, the size of space was set as 45 × 45 × 45 point and other parameter was performed with default of the docking software. Binding energy was displayed. The binding affinities of FTS-IR783 to AMPKα and AMPKβ (**c**), Ras, Akt, GSK3β, and mTOR (**d**) were evaluated using CETSA, the melting curves were fitted by Graphpad with Boltzmann sigmoidal. The binding affinities of FTS to AMPKα and AMPKβ were evaluated using pull-down assay (**e**) and CETSA (**f**), the melting curves were fitted by Graphpad with Boltzmann sigmoidal. **g** Effects of FTS and FTS-IR783 on the in-situ expressions of phospho-AMPKα. **h** The protein expressions of AMPKα, p-AMPKα, AMPKβ, p-AMPKβ, TSC2, and p-TSC2 were detected in MDA-MB-231 cells using Western blotting after FTS-IR783 (1, 2, 4 μM) treatments for 48 h. **i** The protein expressions of AMPKα, p-AMPKα, AMPKβ, p-AMPKβ, TSC2, and p-TSC2 were detected in tumor tissue after FTS-IR783 (1 mg · kg^{-1}) treatments for 14 days. **j** Effects of AMPK inhibitor dorsomorphin on cell viability in MDA-MB-231 cells were observed after dorsomorphin (300 nM) and FTS-IR783 (4 μM) for 48 h. $^{*}P < 0.05$, $^{**}P < 0.01$ and $^{***}P < 0.001$ vs. Model or Ctrl (control). $^{\&}P < 0.05$, $^{\&\&\&}P < 0.001$ vs. FTS-IR783, by two-tailed unpaired Student's *t*-test. The data were shown as Mean ± SD. **k** Effects of AMPK inhibitor dorsomorphin on AMPKα, p-AMPKα, AMPKβ, p-AMPKβ, mTOR, p-mTOR2448, p-mTOR2481, p70S6K, and p-p70S6K expressions.

found that the addition of IR783 changed the drug delivery mechanism and antitumor target of FTS. This provides a reliable reference for further clinical study of the FTS-IR783 conjugate. FTS is one of the most promising agents and the only Ras inhibitor that has ever entered phase II clinical trials [1], and it has shown desirable killing effects on hematologic malignancies and solid tumors [5–7]. However, the high hydrophobicity and poor tumor-targeting capability caused FTS to fail in clinical trials [10, 11]. The results of our study show that the conjugate successfully overcomes the drawbacks of FTS.

Our data indicated that IR783 significantly increased the hydrophilicity of FTS. Lipinski suggested that log *P* values <5 are desirable lipophilicity values for drug candidates, while the optimal log *P* range is between 0 and 3 [32]. Some studies reported that 99% of compounds that display >80% bioavailability fall within this range [33]. In the present study, IR783 significantly increased the hydrophilicity of FTS by ~16.6-fold. The log *P* value of FTS went from 6.393 to 0.384. Importantly, the solubility of FTS-IR783 in water was amplified up to 186 $\mu g \cdot mL^{-1}$ compared to FTS (2 $\mu g \cdot mL^{-1}$) reflecting a highest solubility increase of 93 times.

We revealed that FTS-IR783 showed superior tumor-targeting capability both in vivo and in vitro due to the synergistic effects of OATP transport and endocytosis, which were driven by the predominant role of OATPs and the secondary role of endocytosis. OATPs, a group of membrane-binding solute carriers, play a key role in the uptake of dyes into tumor cells [27]. It has been reported that the uptake of heptamethine cyanine dyes, including IR783 and MHI-148 and their conjugates, are regulated by OATPs [19, 34]. In our study, treatments with the nonselective OATP inhibitor BSP or the OATP1B1 and OATP1B3 inhibitors E2G and CCK8 markedly decreased the uptake of FTS-IR783 in cells. At the same time, we found that 16 proteins that could specifically bind to FTS-IR783 were related to the endocytosis process. Endocytosis, including clathrin-mediated endocytosis, caveolin-mediated endocytosis, clathrin and caveolin-independent endocytosis and macropinocytosis, also plays a key role in macromolecular transport into cells [35]. As expected, treatments with the nonselective endocytic inhibitor sucrose, or the clathrin-mediated and caveolin-mediated endocytosis-selective inhibitors chlorpromazine and methyl-β-cyclodextrin decreased the uptake of FTS-IR783 to varying degrees. In addition, at 90 min after drug treatment, compared with that of FTS-IR783 treatment alone, the inhibition rate of sucrose and BSP treatment alone were 9.5% and 49.43%, respectively, while the inhibition rate of the BSP and sucrose combination treatment was 60.31%, indicating the predominant role of OATPs and the secondary role of endocytosis in the uptake process of FTS-IR783 in cancer cells. Furthermore, the tumor-targeting evaluation results showed that FTS-IR783 accumulated in tumors and was gradually cleared from normal tissues 24 h post-injection. Even at 144 h post-injection, fluorescence was obviously observed in both tumors in mice and isolated tumor tissues. In addition, MCF-7, MDA-MB-231, and 4T1-luc2 breast cancer cells exhibited ~1.5–6-fold higher FTS-IR783 uptake capacity than MCF10A cells.

We also found that FTS-IR783 mainly aggregated in the mitochondria, partially in the lysosome, Golgi apparatus, and endoplasmic reticulum but did not aggregate in the nucleus. Colocalization analysis showed positive correlations between FTS-IR783 and the mitochondria ($r = 0.7779$), lysosome ($r = 0.5793$), endoplasmic reticulum ($r = 0.3240$), and Golgi apparatus ($r = 0.3292$) and negative correlations between FTS-IR783 and the nucleus. This results were further reinforced by the pull-down assay and LC-MS/MS data that FTS-IR783 could bind with proteins related to ribosome (some bound to the membrane of the coarse endoplasmic reticulum or free in cytoplasm), endocytosis (endocytic vesicles are usually fused by lysosomes), protein processing in endoplasmic reticulum and fatty acid metabolism (some are essential for mitochondrial function).

FTS-IR783 indeed showed stronger anti-cancer therapeutic efficacy than FTS both in vivo and in vitro. Successful studies have recently demonstrated that the NIRF dye IR783 could markedly improve cancer cell-targeted delivery and anticancer therapy using anticancer agents, including genistein and nanomedicines [19, 20]. The MTT assay results showed that the IC50 values of FTS-IR783 in these breast cancer cells were 3–10 times lower than those of FTS. Meanwhile, FTS-IR783 more effectively reduced the percentages of EdU-positive cells and colony numbers than FTS by decreasing the expression of the cell proliferation markers PCNA [25] and Ki67 [36] in breast cancer cells. On the other hand, FTS-IR783 produced stronger inhibition of 4T1-luc2 and MDA-MB-231 cell migration than FTS and reduced the protein levels of the EMT-related markers N-cadherin and vimentin [26]. In our study, the antitumor effects of FTS-IR783 (30 $mg \cdot kg^{-1}$) on tumor growth and tumor pulmonary metastasis suppression were both ~2 times stronger than those of FTS (10 $mg \cdot kg^{-1}$) at an equal dose in vivo. In addition, the pharmacokinetic profiles were explored to further confirm why the antitumor efficacy of FTS-IR783 in vitro was stronger than that in vivo compared with FTS. Compared with FTS, although the C_{max} of FTS-IR783 was decreased, the $t_{1/2}$, AUC_{0-t}, $AUC_{0-\infty}$, V_d and MRT_{0-t} of FTS-IR783 were both significantly increased. The longer retention time made the relative bioavailability of FTS-IR783 increase by 90.7% compared with FTS, which was consistent with the antitumor effects of FTS-IR783 and FTS in vivo. Moreover, in addition to good anti-tumor therapeutic efficacy, FTS-IR783 also presented low systemic toxicity without remarkably altering the average body weight, tissue indexes and tissue structures of the liver, spleen and kidney.

We demonstrated that the conjugation of IR783 improved the anticancer activity of FTS by altering the mechanism. FTS treatment downregulated the expressions of Ras, Akt, p-Akt, ERK, and p-ERK, which was consistent with reports that FTS could inhibit cell proliferation and metastasis through the Raf/MEK/ERK and PI3K/Akt/mTOR signaling pathways [8, 9]. In contrast, FTS-IR783 treatments had no significant effect on Ras, Akt, p-Akt, and ERK1/2 protein expressions but inhibited the expression of p-ERK1/2, suggesting that the anticancer molecular mechanism of FTS-IR783 was different from that of FTS. FTS-IR783 was aggregated in the cytoplasm, especially in mitochondria, but not in the nucleus. Also, the pull-down assay and LC-MS/MS results showed 331 proteins which specifically bind to FTS-IR783 were mainly distributed in cytoplasm. Moreover, FTS-IR783 could bind with the AMPK β subunit. AMPK is a heterotrimeric protein complex that is formed by the α, β, and γ subunits [37]. AMPK is a critically important cellular energy sensor and metabolic regulator which plays a critical role in mitochondria quality control [38]. Importantly, FTS-IR783 could bind with the AMPK α and β subunits rather than Ras. Conversely, FTS showed no affinity for the AMPK α and β subunits, indicating that after conjugation with IR783, the target of the conjugate was changed. It is well known that activated AMPK promotes TSC activation and inhibits mTOR signal transduction [31]. We also found that FTS had no effect on in-situ expression of phospho-AMPK, while FTS-IR783 dose-dependently enhanced the phosphorylation levels of the AMPK α and β subunits both in vitro and in vivo. Consistently, FTS-IR783 treatments significantly increased the phosphorylation of TSC2 and suppressed the mTOR signaling pathway both in vitro and in vivo. Furthermore, the AMPK inhibitor dorsomorphin reversed the inhibitory effects of FTS-IR783 on AMPK activation, the mTOR pathway and cancer cell viability. Moreover, FTS-IR783 mTOR-dependently suppressed breast cancer progression by inhibiting p-mTOR expression more strongly than FTS. Taken together, the results proved that FTS-IR783 shows stronger antitumor activity than FTS by regulating the AMPK/TSC2/mTOR signaling pathway without influencing Ras.

Our data highlight a promising approach for the modification of the antitumor drug FTS using the NIRF dye IR783 and may be possible to return FTS back to the clinic with a better efficacy. The novel strategy that IR783 increases therapeutic efficacy and lead to a targeting change of FTS, bringing rethink on drug modification research. Additionally, for the first time we found that OATP transport and endocytosis synergistically mediated the delivery of the tumor-targeting drug FTS-IR783, providing a new theoretical basis for the mechanism studies of clinical tumor-targeting drugs.

ACKNOWLEDGEMENTS

This work was supported by the projects of National Natural Science Foundation of China [81720108033, 81930114, and 81874367], Natural Science Foundation of Guangdong Province [2018B030322011], and Natural Science Foundation for Distinguished Young Scholars of Guangdong Province [2017A030306033].

AUTHOR CONTRIBUTIONS

ZQL and LLL conceived the ideas and designed the experiments. QJH, MLY, JHD, JJY, YMZ, XRZ performed the experiments and analyzed the data. QJH prepared the manuscript. ZQL, LLL, FXZ, and GCL provided critical revisions to the manuscript. YW, XXQ, ZYH, DFP, and YG provided technical supports. All authors read and agreed on the final version of the manuscript.

ADDITIONAL INFORMATION

Supplementary information The online version contains supplementary material available at https://doi.org/10.1038/s41401-021-00775-5.

Competing interests: The authors declare no competing interests.

REFERENCES

1. Wang Y, Kaiser CE, Frett B, Li HY. Targeting mutant KRAS for anticancer therapeutics: a review of novel small molecule modulators. J Med Chem. 2013;56:5219–30.
2. Holderfield M, Morrison DK. RAS signaling: divide and conquer. Nat Chem Biol. 2016;13:7–8.
3. Kwong LN, Costello JC, Liu H, Jiang S, Helms TL, Langsdorf AE, et al. Oncogenic NRAS signaling differentially regulates survival and proliferation in melanoma. Nat Med. 2012;18:1503–10.
4. Ledford H. Cancer: the Ras renaissance. Nature. 2015;520:278–80.
5. Laheru D, Shah P, Rajeshkumar NV, McAllister F, Taylor G, Goldsweig H, et al. Integrated preclinical and clinical development of S-trans, trans-Farnesylthiosalicylic Acid (FTS, Salirasib) in pancreatic cancer. Invest N Drugs. 2012;30:2391–9.
6. Santen RJ, Lynch AR, Neal LR, McPherson RA, Yue W. Farnesylthiosalicylic acid: inhibition of proliferation and enhancement of apoptosis of hormone-dependent breast cancer cells. Anticancer Drugs. 2006;17:33–40.
7. Zundelevich A, Elad-Sfadia G, Haklai R, Kloog Y. Suppression of lung cancer tumor growth in a nude mouse model by the Ras inhibitor salirasib (farnesylthiosalicylic acid). Mol Cancer Ther. 2007;6:1765–73.
8. Bustinza-Linares E, Kurzrock R, Tsimberidou AM. Salirasib in the treatment of pancreatic cancer. Future Oncol. 2010;6:885–91.
9. Yue W, Wang J, Li Y, Fan P, Santen RJ. Farnesylthiosalicylic acid blocks mammalian target of rapamycin signaling in breast cancer cells. Int J Cancer. 2005;117:746–54.
10. Badar T, Cortes JE, Ravandi F, O'Brien S, Verstovsek S, Garcia-Manero G, et al. Phase I study of S-trans, trans-farnesylthiosalicylic acid (salirasib), a novel oral RAS inhibitor in patients with refractory hematologic malignancies. Clin Lymphoma Myeloma Leuk. 2015;15:433–438.e2.
11. Furuse J, Kurata T, Okano N, Fujisaka Y, Naruge D, Shimizu T, et al. An early clinical trial of Salirasib, an oral RAS inhibitor, in Japanese patients with relapsed/refractory solid tumors. Cancer Chemother Pharmacol. 2018;82:511–9.
12. Riely GJ, Johnson ML, Medina C, Rizvi NA, Miller VA, Kris MG, et al. A phase II trial of Salirasib in patients with lung adenocarcinomas with KRAS mutations. J Thorac Oncol. 2011;6:1435–7.
13. Tsimberidou AM, Rudek MA, Hong D, Ng CS, Blair J, Goldsweig H, et al. Phase 1 first-in-human clinical study of S-trans, trans-farnesylthiosalicylic acid (salirasib) in patients with solid tumors. Cancer Chemother Pharmacol. 2010;65:235–41.
14. Yang X, Shao C, Wang R, Chu CY, Hu P, Master V, et al. Optical imaging of kidney cancer with novel near infrared heptamethine carbocyanine fluorescent dyes. J Urol. 2013;189:702–10.
15. Yi X, Wang F, Qin W, Yang X, Yuan J. Near-infrared fluorescent probes in cancer imaging and therapy: an emerging field. Int J Nanomed. 2014;9:1347–65.
16. Yang X, Shi C, Tong R, Qian W, Zhau HE, Wang R, et al. Near IR heptamethine cyanine dye-mediated cancer imaging. Clin Cancer Res. 2010;16:2833–44.
17. James NS, Chen Y, Joshi P, Ohulchanskyy TY, Ethirajan M, Henary M, et al. Evaluation of polymethine dyes as potential probes for near infrared fluorescence imaging of tumors: part - 1. Theranostics. 2013;3:692–702.
18. Duan L, Wang L, Zhang C, Yu L, Guo F, Sun Z, et al. Role of near-infrared heptamethine cyanine dye IR-783 in diagnosis of cervical cancer and its mechanism. Int J Clin Exp Pathol. 2019;12:2353–62.
19. Guan Y, Zhang Y, Zou J, Huang LP, Chordia MD, Yue W, et al. Synthesis and biological evaluation of genistein-IR783 conjugate: cancer cell targeted delivery in MCF-7 for superior anti-cancer therapy. Molecules. 2019;24:4120.
20. Zhang B, Wang H, Shen S, She X, Shi W, Chen J, et al. Fibrin-targeting peptide CREKA-conjugated multi-walled carbon nanotubes for self-amplified photothermal therapy of tumor. Biomaterials. 2016;79:46–55.
21. Almqvist H, Axelsson H, Jafari R, Dan C, Mateus A, Haraldsson M, et al. CETSA screening identifies known and novel thymidylate synthase inhibitors and slow intracellular activation of 5-fluorouracil. Nat Commun. 2016;7:11040.
22. Martinez Molina D, Jafari R, Ignatushchenko M, Seki T, Larsson EA, Dan C, et al. Monitoring drug target engagement in cells and tissues using the cellular thermal shift assay. Science. 2013;341:84–87.
23. Zhai HY, Liu ZP, Chen ZG, Liang ZX, Su ZH, Wang SM. A sensitive electrochemical sensor with sulfonated graphene sheets/oxygen-functionalized multi-walled carbon nanotubes modified electrode for the detection of clenbuterol. Sens Actuators B-Chem. 2015;210:483–90.
24. Williams HD, Trevaskis NL, Charman SA, Shanker RM, Charman WN, Pouton CW, et al. Strategies to address low drug solubility in discovery and development. Pharmacol Rev. 2013;65:315–499.
25. Wang SC. PCNA: a silent housekeeper or a potential therapeutic target? Trends Pharmacol Sci. 2014;35:178–86.
26. Zhu GJ, Song PP, Zhou H, Shen XH, Wang JG, Ma XF, et al. Role of epithelial-mesenchymal transition markers E-cadherin, N-cadherin, beta-catenin and ZEB2 in laryngeal squamous cell carcinoma. Oncol Lett. 2018;15:3472–81.
27. Wu JB, Shi C, Chu GC, Xu Q, Zhang Y, Li Q, et al. Near-infrared fluorescence heptamethine carbocyanine dyes mediate imaging and targeted drug delivery for human brain tumor. Biomaterials. 2015;67:1–10.
28. Letschert K, Faulstich H, Keller D, Keppler D. Molecular characterization and inhibition of amanitin uptake into human hepatocytes. Toxicol Sci. 2006;91:140–9.
29. Tian T, Li X, Zhang J. mTOR signaling in cancer and mTOR inhibitors in solid tumor targeting therapy. Int J Mol Sci. 2019;20:755.
30. McMahon LP, Yue W, Santen RJ, Lawrence JC Jr. Farnesylthiosalicylic acid inhibits mammalian target of rapamycin (mTOR) activity both in cells and in vitro by promoting dissociation of the mTOR-raptor complex. Mol Endocrinol. 2005;19:175–83.
31. Wang H, Liu Y, Wang D, Xu Y, Dong R, Yang Y, et al. The upstream pathway of mTOR-mediated autophagy in liver diseases. Cells. 2019;8:1597.
32. Waring MJ. Lipophilicity in drug discovery. Expert Opin Drug Discov. 2010;5:235–48.
33. Lindsley CW Lipophilicity. In: Stolerman I, Price L, editors. Encyclopedia of Psychopharmacology. Berlin; Heidelberg: Springer; 2014.
34. Shi C, Wu JB, Chu GC, Li Q, Wang R, Zhang C, et al. Heptamethine carbocyanine dye-mediated near-infrared imaging of canine and human cancers through the HIF-1alpha/OATPs signaling axis. Oncotarget. 2014;5:10114–26.
35. Bruce A, Alexander J, Julian L, Martin R, Keith R, & Peter W. Transport into the cell from the plasma membrane: endocytosis. Molecular Biology of the Cell. 4th ed. New York: Garland Science; 2002.
36. Miller I, Min M, Yang C, Tian C, Gookin S, Carter D, et al. Ki67 is a graded rather than a binary marker of proliferation versus quiescence. Cell Rep. 2018;24:1105–1112.e5.
37. Stapleton D, Mitchelhill KI, Gao G, Widmer J, Michell BJ, Teh T, et al. Mammalian AMP-activated protein kinase subfamily. J Biol Chem. 1996;271:611–4.
38. Zhang H, Liu B, Li T, Zhu Y, Luo G, Jiang Y, et al. AMPK activation serves a critical role in mitochondria quality control via modulating mitophagy in the heart under chronic hypoxia. Int J Mol Med. 2018;41:69–76.